Microstructure and thermoelectric properties of CrN and CrN/Cr 2 N thin films

M Gharavi, S Kerdsongpanya, S. Schmidt, F Eriksson, N Nong, J. Lu, B Balke, D. Fournier, Laurent Belliard, A. Le Febvrier, et al.

To cite this version:

M Gharavi, S Kerdsongpanya, S. Schmidt, F Eriksson, N Nong, et al.. Microstructure and thermoelectric properties of CrN and CrN/Cr 2 N thin films. Journal of Physics D: Applied Physics, 2018, 51 (35), pp.355302. ⟨10.1088/1361-6463/aad2ef⟩. ⟨hal-02457466⟩

HAL Id: hal-02457466
https://hal.science/hal-02457466v1

Submitted on 3 Jul 2025

Journal of Physics D:
Applied Physics

PAPER • **OPEN ACCESS**

Microstructure and thermoelectric properties of CrN and CrN/Cr_2N thin films

To cite this article: M A Gharavi *et al* 2018 *J. Phys. D: Appl. Phys.* **51** 355302

OPEN ACCESS
IOP Publishing

Journal of Physics D: Applied Physics

J. Phys. D: Appl. Phys. **51** (2018) 355302 (9pp)

https://doi.org/10.1088/1361-6463/aad2ef

Microstructure and thermoelectric properties of CrN and CrN/Cr_2N thin films

M A Gharavi[1,6], S Kerdsongpanya[1,2], S Schmidt[1], F Eriksson[1], N V Nong[3], J Lu[1], B Balke[4], D Fournier[5], L Belliard[5], A le Febvrier[1], C Pallier[1] and P Eklund[1]

[1] Department of Physics, Thin Film Physics Division, Chemistry and Biology (IFM), Linköping University, SE-581 83 Linköping, Sweden
[2] Department of Materials Science and Engineering, Rensselaer Polytechnic Institute, Troy, NY 12180, United States of America
[3] Department of Energy Conversion and Storage, Technical University of Denmark, DK-4000 Roskilde, Denmark
[4] Institute of Inorganic and Analytical Chemistry, Johannes Gutenberg University, D-55131 Mainz, Germany
[5] Institut des NanoSciences de Paris, Sorbonne Universités, UPMC Universités Paris 06, UMR 7588, Paris F-75005, France

E-mail: mohammad.amin.gharavi@liu.se

Received 14 March 2018, revised 31 May 2018
Accepted for publication 12 July 2018
Published 2 August 2018

Abstract

CrN thin films with an N/Cr ratio of 95% were deposited by reactive magnetron sputtering onto (0 0 0 1) sapphire substrates. X-ray diffraction and pole figure texture analysis show CrN (1 1 1) epitaxial growth in a twin domain fashion. By changing the nitrogen versus argon gas flow mixture and the deposition temperature, thin films with different surface morphologies ranging from grainy rough textures to flat and smooth films were prepared. These parameters can also affect the CrN_x system, with the film compound changing between semiconducting CrN and metallic Cr_2N through the regulation of the nitrogen content of the gas flow and the deposition temperature at a constant deposition pressure. Thermoelectric measurements (electrical resistivity and Seebeck coefficient), scanning electron microscopy, and transmission electron microscopy imaging confirm the changing electrical resistivity between 0.75 and 300 $\mathrm{m\,\Omega\,cm}$, the changing Seebeck coefficient values between 140 and 230 $\mu\,\mathrm{VK}^{-1}$, and the differences in surface morphology and microstructure as higher temperatures result in lower electrical resistivity while gas flow mixtures with higher nitrogen content result in single phase cubic CrN.

Keywords: magnetron sputtering, thermoelectrics, chromium nitride, seebeck coefficient, thin films

S Supplementary material for this article is available online

(Some figures may appear in colour only in the online journal)

---

[6] Author to whom any correspondence should be addressed.

1. Introduction

Chromium nitride (CrN) is a hard and corrosion resistant compound that has gained interest for various applications such as medical implants [1], silver luster decorative coatings [2], and wear-resistant coatings for cutting tools especially when hot corrosion resistance is needed [3, 4]. Chromium nitride is an interstitial compound, in which nitrogen atoms reside in the octahedral spaces between the chromium atoms in an fcc lattice (i.e. rock-salt cubic), making the compound susceptible to stoichiometry deficiency. There is also a second interstitial compound, hexagonal Cr_2N, which can be formed in CrN films as a secondary phase [5, 6]. In addition to the more traditional applications and properties of CrN, studies on the thermoelectric properties have shown that CrN has a moderate electrical resistivity, low thermal conductivity, and high Seebeck coefficient values. Quintela *et al* [7] reported on 1:1 stoichiometric CrN thin films, showing a Seebeck coefficient of approximately $-120\ \mu\mathrm{VK}^{-1}$ and a dimensionless figure of merit (zT) of 0.12 at room temperature (compared to 0.1 for PbTe:Tl). Their work emphasizes the fact that annealed samples have better electrical and thermal conductivity, resulting in films with enhanced thermoelectric properties. Kerdsongpanya *et al* [8] reported a Seebeck coefficient of $-230\ \mu\mathrm{VK}^{-1}$ and a power factor of $1.7 \times 10^{-3}\ \mathrm{Wm}^{-1}\ \mathrm{K}^{-2}$ near 400 °C for CrN thin films deposited on sapphire by magnetron sputtering. The high electrical resistivity of CrN stems from the localized $3d$ orbitals which give the electrons large effective masses and consequently high electrical resistivity and low thermal conductivity (between 1.7 and 4.0 $\mathrm{Wm}^{-1}\ \mathrm{K}^{-1}$) [9–11]. With CrN oxidizing at 700 °C and the thermal decomposition (in an inert atmosphere) starting at 1000 °C, CrN has the potential to be a suitable n-type semiconductor for mid-to-high temperature thermoelectrics. As for semiconducting properties, previous reports have announced different band gaps for CrN. Constantin *et al* [12] prepared 1:1 stoichiometric CrN thin films deposited by molecular beam epitaxy, and reported a resistivity-derived 71 meV band gap at room temperature, by using the $\ln(\rho/\rho_0) = (E_g/2k_B)(1/T)$ equation which relates the resistivity of a semiconductor to ambient temperature and the energy band gap where ρ is the electrical resistivity, ρ_0 is the resistivity pre-factor, E_g is the semiconductor band gap, k_B is the Boltzmann constant and T is temperature. Zhang *et al* [13] measured the optical properties of CrN and concluded that the band gap is 0.19 eV with an error bar of 0.46 eV, demonstrating difficulties in this regard. On the other hand, at low temperatures the resistivity of CrN indicates metallic properties [14]. This is explained by a magnetic phase transformation at the Néel temperature (approximately 280 K), which causes antiferromagnetic orthorhombic CrN to transform into paramagnetic rock-salt cubic CrN with temperature increase. Adding N vacancies and/or other defects coupled with a narrow band gap will increase the charge carrier density resulting in metallic conducting properties [15–17]. Gall *et al* [18] measured an optical band gap of approximately 0.7 eV and conclude that the semiconducting properties stem from the existence of magnetic moments and the Hubbard energy rather than the crystal structure, indicating a Mott insulator. They also noted that depending on crystal quality, the temperature dependence of electrical resistivity ($d\rho/dT$) may either be positive or negative for the low-temperature orthorhombic phase.

In general, these studies have led researchers to propose chromium nitride as a possible thermoelectric material in addition to other traditional thermoelectric materials which are limited to niche applications [19]. For example, products based on bismuth telluride (Bi_2Te_3), which has one of the highest zT values at room temperature (approximately 1), and lead telluride (PbTe), which operates with a significant zT of 1.4 at 500 °C, are both restricted because of the low global production of tellurium [20, 21]. As a result, the chemical stability and mechanical properties of CrN could address this and other limiting factors [22–24].

In order to optimize semiconductors for thermoelectric properties and expand their use in a wider range of high temperature applications, cheaper and more stable materials like CrN should be explored. Nitride thin films (and other thermoelectric material) can be optimized by adding dopants, synthesizing semiconductor/metal multilayers and nanostructuring, leading to the simultaneous decrease of the electrical resistivity and the thermal conductivity [25, 26] and resulting an improved thermoelectric performance (or figure-of-merit). The interest in using thermoelectrics based on early transition-metal nitrides is further underlined by the results on ScN-based materials, both pure ScN [27–31], ScN-based solid solutions and alloys [32–34], and superlattices [35–37].

The thermoelectric properties of CrN (which can be further enhanced by alloying [38]) present this material as a promising semiconductor for use in mid-temperature thermoelectric applications. However, the effects of the microstructure and the CrN_x system on the thermoelectric properties are not well understood as both properties can affect the electronic band structure (hence the Seebeck coefficient), electrical resistivity and thermal conductivity (by phonon scattering). Here, we study the effects of film microstructure and phase purity on the Seebeck coefficient, electrical resistivity and thermal conductivity. CrN thin film quality may have a profound effect on the electrical conductivity by reducing charge carrier scattering at the grain boundaries and the existence of the secondary phase Cr_2N can be used to alter the electrical conductivity and modify the thermoelectric efficiency leading to a higher power factor value.

2. Experimental details

The deposition process was carried out by reactive dc magnetron sputtering in a high vacuum chamber base pressure (3.0×10^{-7} mbar at deposition temperature). The films were deposited onto (0 0 0 1) sapphire substrates ($10 \times 10 \times 0.5\ \mathrm{mm}^3$, ultrasonically cleaned in acetone and isopropanol 5 min each and blown dry using N_2) that were heated at 600, 650 and 700 °C for 1 h prior to the deposition process. These temperatures were also maintained during the deposition process. The 300 nm thick films were deposited using a 7.5 cm Cr (Lesker, 99.95% pure) target and an argon/nitrogen gas mixture (99.9997% pure for both gases). The target power for chromium was kept constant and set at 50 W under a constant deposition pressure of 0.6 Pa (4.5 mTorr). Details of the deposition setup can be found elsewhere [39]. The substrate holder was rotated with a speed of 17 rpm and was grounded. The deposition time was 90 min for the 20% nitrogen gas mixture (11 sccm N_2, 43 sccm Ar) and 120 min for the 40% nitrogen gas mixture (21 sccm N_2, 33 sccm Ar) in order to maintain equal thickness.

High resolution x-ray diffraction (HRXRD) $\theta - 2\theta$ scans were carried out in a PANalytical Empyrean diffractometer (line focus mode) equipped with a Cu $K\alpha$ source operated at 45 kV and 40 mA. The incident optics was a hybrid monochromator 2 bounce Ge (2 2 0) module including a 0.5° divergence slit, and the diffracted optics was a 3 bounce Ge (2 2 0) symmetrical analyzer. The XRD step sizes and collection times per step were 0.001° and 0.8 s, respectively. Pole figure measurements were performed in the same diffractometer operated at 45 kV and 40 mA (point focus mode) with a 2×2 mm^2 crossed slit x-ray lens and a parallel plate collimator as the incident and diffracted beam optics, respectively. Pole figures of the CrN (1 1 1) peak were acquired in the tilt-angle (ψ) range between 0 and 85° and azimuth-angle (φ) range between 0 and 360° with steps of 5° for both ψ and φ and a collection time of 1 s. Atomic force microscopy (AFM) was performed using a Brüker Dimension 3100 AFM in tapping mode and the data was processed by WS × M analysis software [40] and include a ±1 nm instrumental error bar in the Z axis.

The chemical composition of the CrN films was studied using x-ray photoelectron spectroscopy (XPS, Axis UltraDLD, Kratos Analytical, UK) equipped with a monochromatic Al (K_α) x-ray radiation ($h\nu = 1486.6$ eV) source. The base pressure in the analysis chamber during acquisition was less than 1×10^{-9} mbar. Survey spectra as well as XPS core level spectra of the Cr 2p, N 1s, and O 1s regions were recorded on as-deposited samples and after sputter cleaning for 600 s with a 0.5 keV Ar^+ ion beam. The Ar^+ beam had an incidence angle of 20° and was rastered over an area of 3×3 mm^2. Sputter cleaning was carried out to remove the surface oxygen layer that grows upon air exposure. The core level spectra recorded after Ar^+ etching was used to extract the chemical composition of the CrN coatings. Here, a Shirley-type background was subtracted, and elemental cross sections provided by Kratos Analytical were applied. Preferential sputtering of the nitrogen species and film surface roughness is also taken into consideration [41], thus resulting a 3% error bar in the quantitative measurements.

A JEOL 2200FS operating at 200 kV was used for transmission electron microscopy (TEM). Cross-sectional samples for the TEM were prepared by mechanically polishing them to down to 55 μm by hand. Ion milling was then applied using a Gatan precision ion polishing system (PIPS) with a 5 keV Ar^+ ion beam angled at 8° of incidence relative to the sample surface for 2 h and 5° for 4 h. Once electron transparency was reached, a final ion milling step was applied with lower energy ion beams (2 keV) for 30 min.

Sample thickness and surface morphologies were obtained by a LEO 1550 Gemini scanning electron microscope (SEM). The acceleration voltage was set to 5 KV and the cross-sectional SEM image thickness measurement includes a ±10 nm error bar (~3%). Cross-sectional SEM images are available in the supplementary material (stacks.iop.org/JPhysD/51/355302/mmedia).

The electrical resistivity of all samples was obtained by measuring the sheet resistance of the films with a four-point-probe Jandel RM3000 station and multiplying the sheet resistance with the film thickness (obtained from cross sectional SEM imaging). In-plane electrical resistivity and Seebeck coefficient value measurements of CrN and CrN/Cr_2N samples were simultaneously performed from room temperature up to 800 K by an Ulvac-Riko Zem 3 system with a special setup for thin film measurements in a low-pressure helium atmosphere. The measurement error is no more than 7% for this setup as mentioned in [8]. Temperature-dependent Hall carrier concentrations were determined on 5×5 mm^2 substrates using the IPM-HT Hall-900 K system (developed and constructed by Fraunhofer IPM in Freiburg, Germany) and includes a 10% error bar. Thermal conductivity of CrN and Cr_2N was determined by modulated thermoreflectance microscopy (MTRM). In this setup, a pump beam at 532 nm (delivered by a Cobolt Samba MLD laser and with the intensity modulated by an acousto-optical modulator at a frequency f) is focused on the surface of the sample with an objective lens (N.A. = 0.5). The samples were coated by a 100 nm gold layer, ensuring that the heat source is located at the surface. Thermal waves are excited in the sample and monitored by the reflectivity surface change recorded around the pump location by another focused laser beam. A 488 nm Oxius laser is used to maximize the probe sensitivity towards the thermal field in the gold cap layer. A photodiode and a lock-in amplifier recorded the AC reflectivity component, in a frequency range between 1 kHz and 1 MHz. Finally, the experimental profiles of the amplitude and the phase of the reflected probe beam were fitted according to a standard Fourier diffusion law to extract the thermal conductivity of the films and includes a measurement error of 15% [42–48].

3. Results

3.1. Initial experiments

The main growth parameters for the reactive sputter-deposition of chromium nitride were the substrate deposition temperature (kept constant for 1 h before initiating the growth process) and the argon/nitrogen gas flow mixture. In an initial study of deposition temperature, we observed that low temperature deposition at 550 °C or lower will lead to the formation of polycrystalline films with high electrical resistivity, while deposition temperatures higher than 700 °C typically results in predominant growth of Cr_2N over cubic CrN consistent with earlier observations [49]. Thus, we limit the presentation of experiments below to the most important temperature ranges between 600 °C and 700 °C.

The gas flow mixture of argon and nitrogen also affected the films. A 60% argon and 40% nitrogen gas flow mixture resulted in sharp CrN (1 1 1) XRD peaks. However, an 80%

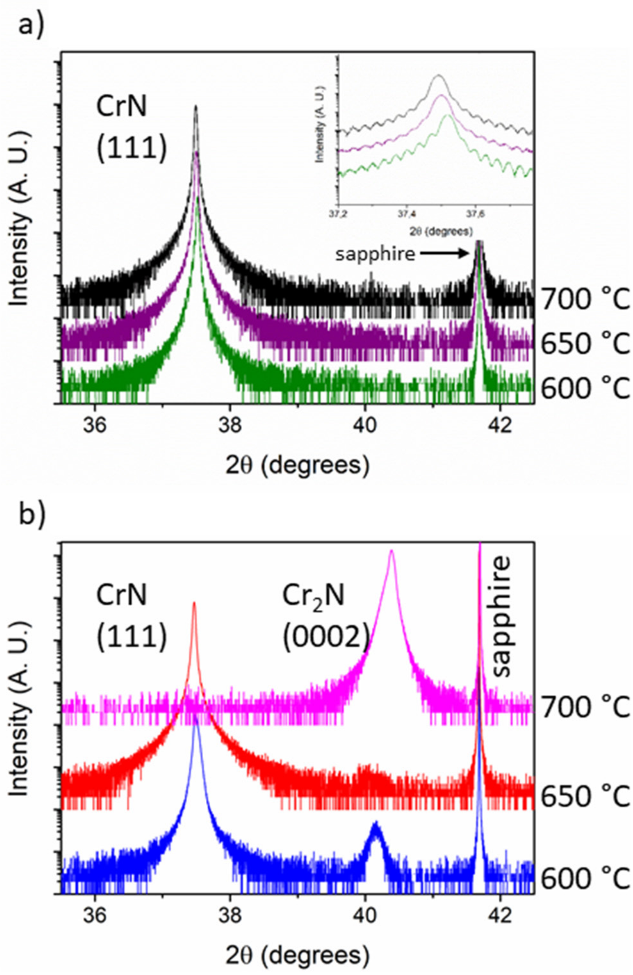

Figure 1. XRD diffractograms of CrN–Cr_2N films deposited at 600, 650 and 700 °C: (a) with a 40% nitrogen gas mixture and (b) with a 20% nitrogen gas mixture. The inset shows a zoomed image of the CrN (1 1 1) peak. The fringes are so called Laue oscillations (layer thickness fringes).

argon and 20% nitrogen gas flow mixture led to the formation of the Cr_2N phase. Thus, the 20% nitrogen gas mixture (11 sccm N_2, 43 sccm Ar) is used to study phase mixtures of CrN and Cr_2N while as the 40% nitrogen gas mixture (21 sccm N_2, 33 sccm Ar) results in single phase CrN. The aim of this research is to study the thermoelectric properties of chromium nitride showing this phase variation: CrN, Cr_2N and CrN/Cr_2N.

3.2. Effects of process parameters on CrN film growth

Figure 1(a) shows $\theta - 2\theta$ diffractograms for a set of CrN thin films deposited at 600 °C, 650 °C, and 700 °C under the conditions of a 40% nitrogen gas mixture and a grounded substrate. In addition, XPS measurements show that all the studied CrN films are sub-stoichiometric, with $N = 45\%$ and $Cr = 55\%$ (considering a 3% error bar). XPS spectra for all samples are available in the supplementary material. These values match the elastic recoil detection analysis (ERDA) values obtained by Kerdsongpanya *et al* [8] for similar samples deposited in the same PVD system. As for the single phase Cr_2N films, the approximate stoichiometry is $N = 69\%$ and $Cr = 30\%$. Oxygen contamination of all films was measured to be less than 2%.

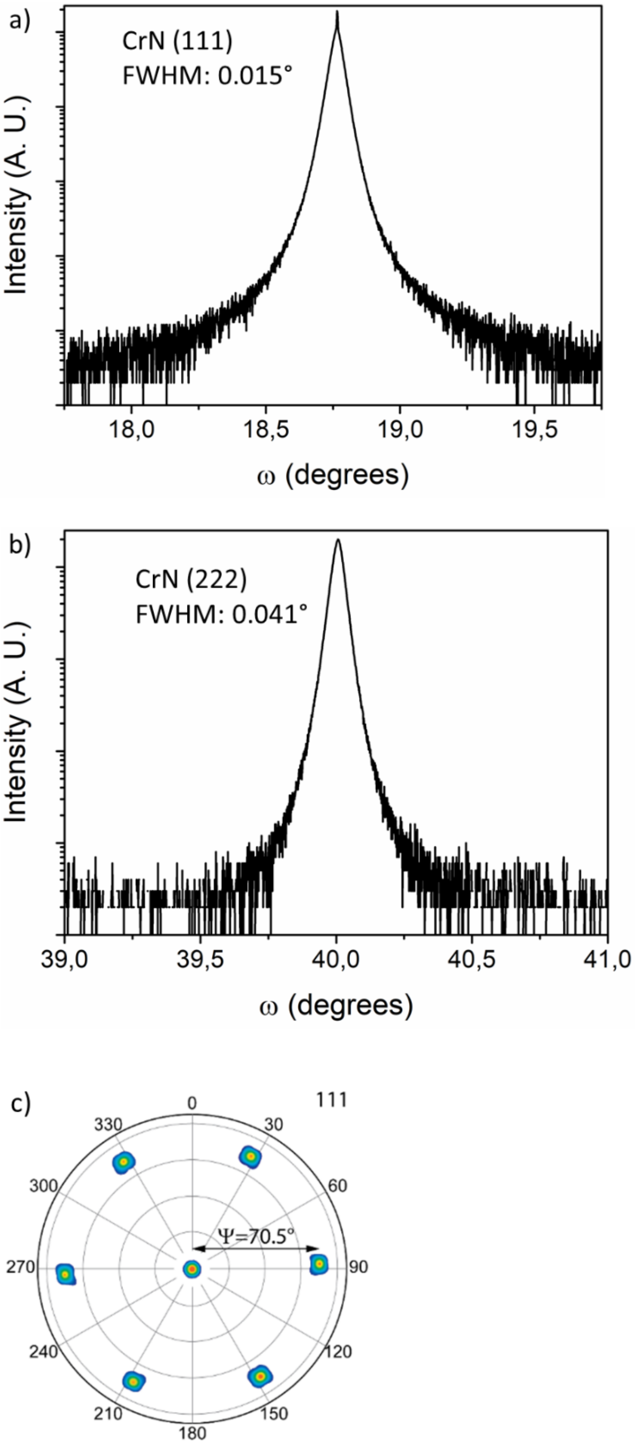

Figure 2. Rocking curve measurements of single phase CrN deposited at 700 °C. (a) Rocking curve scan of CrN (1 1 1). (b) Rocking curve scan of CrN (2 2 2). (c) Pole figure analysis for the CrN (1 1 1) peak measured on sample Cr40-700.

The diffraction pattern shows the CrN (1 1 1) peak located at $2\theta = 37.49°$ corresponding to a 0.23 nm lattice spacing. The peak located at $2\theta = 41.69°$ is the sapphire (0 0 0 6) substrate peak. The inset shows a zoomed image of the CrN (1 1 1) peak. The fringes are so called Laue oscillations (layer thickness fringes) which appear only for very smooth films, and the separation of these correspond to the film thickness.

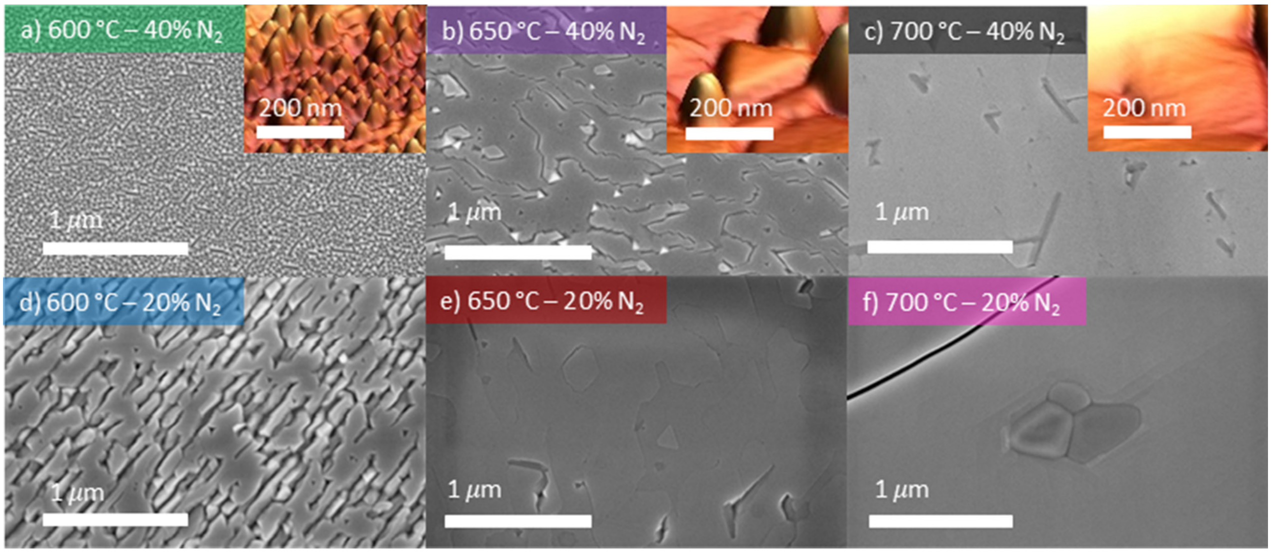

Figure 3. SEM images of epitaxial CrN-Cr$_2$N thin films deposited at 600, 650 and 700 °C. 40% nitrogen gas mixture for images (a)–(c) and 20% nitrogen gas mixture for images (d)–(f). The insets in images (a)–(c) belong to AFM measurements performed on the single phase CrN samples.

Table 1. Deposition temperature, nitrogen gas flow mixture, roughness measurement, electrical resistivity and charge carrier concentration measurements for samples shown in figures 1 and 2.

				Roughness				n ($\times 10^{18}$ cm^{-3})	
Sample name	N$_2$ gas (%)	Deposition temp. °C	Phase and thickness	Rq (nm)	Peak to peak (nm)	ρ at RT ($\mu\Omega \cdot$ cm)	k at RT (W $\cdot$ m^{-1} K^{-1})	300 K	800 K
Cr40-700	40	700	Cubic CrN 280 nm	3	18	750	4.0	39	172
Cr40-650		650	Cubic CrN 280 nm	8	50	300 000	—	—	—
Cr40-600		600	Cubic CrN 280 nm	5	29	300 000	—	—	—
Cr20-700	20	700	Hex. Cr$_2$N 280 nm	—	—	50	12.0	81 700	287 000
Cr20-650		650	CrN/Cr$_2$N 310 nm	—	—	830	—	42	193
Cr20-600		600	CrN/Cr$_2$N 320 nm	—	—	1300	—	310	1190

Figure 1(b) shows $\theta - 2\theta$ diffractograms for a similar set of samples when deposited with 20% nitrogen gas flow mixture. At 600 °C, a Cr$_2$N (0 0 0 2) phase impurity peak (with a smaller intensity compared to the CrN peak) is seen at approximately $2\theta \approx 40°$. Increasing the deposition temperature to 650 °C decreases the Cr$_2$N (0 0 0 2) peak intensity, while an increase to 700 °C will result in single-phase Cr$_2$N.

Figures 2(a) and (b) shows rocking curve measurements of single phase CrN (1 1 1) deposited at 700 °C comparing the full width at half maximum (FWHM) of the (1 1 1) and (2 2 2) peaks. The FWHM for CrN (1 1 1) is 0.015° compared to the 0.041° for CrN (2 2 2), indicating the existence of mosaicity. Figure 2(c) is a pole figure of the CrN {1 1 1} peaks (single phase CrN, deposited at 700 °C) and includes six equally distanced and discrete poles surrounding the central pole at $\psi = 70.5°$ which is the angle between {1 1 1} crystal planes in a cubic crystal structure. A single crystal fcc structures deposited in the [1 1 1] direction should only show three surrounding poles, indicating a twin domain epitaxial growth (where the domains are rotated 60° with respect to each other) [50], a well-known feature for cubic material deposited on sapphire.

Figure 3 shows the SEM images of the samples corresponding to the diffraction patterns in figure 1. These images show a temperature-activated change in the surface morphology. The insets in figures 3(a)–(c) present the AFM measurements performed on single phase CrN (samples Cr40-600, Cr40-650 and Cr40-700). The SEM and AFM results show that the film deposited at 600 °C is composed of many small triangular grains growing in the (1 1 1) direction as determined by the XRD pattern and with an approximate size of 50 nm. As the temperature increases towards 700 °C, SEM images show large micrometer-sized grains and grain boundaries which originates from the twin domain nature of the film. Figures 3(d)–(f) show the SEM images of the samples deposited with a 20% nitrogen gas mixture (samples Cr20-600, Cr20-650 and Cr20-700). These images show that Cr20-600, which has a larger amount of Cr$_2$N mixed inside the CrN matrix (compared to Cr20-650) leads to a dented surface and multiple surface features. On the other hand, Cr20-700 (which is single phase Cr$_2$N) has less of such features.

Table 1 lists sample features according to their processing parameters, compound phase, roughness analysis, electrical resistivity, and charge carrier density values. Although the samples Cr40-600, Cr40-650 and Cr40-700 (deposited with a 40% N$_2$ gas mixture) are single phase and nearly stoichiometric (N/Cr ~ 95%), the four-point-probe measurements

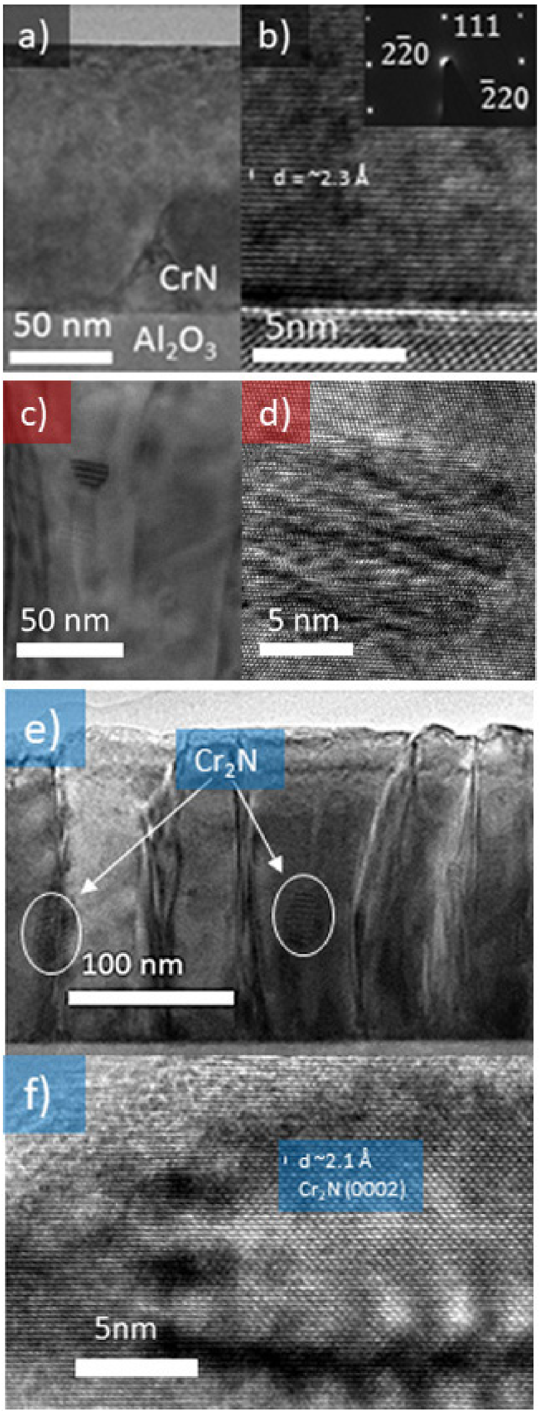

Figure 4. (a) TEM and (b) HRTEM and SAED image of single phase, epitaxial CrN deposited at 700 °C with a 40% nitrogen gas mixture. (c) TEM and (d) HRTEM image of a hexagonal Cr_2N nanoinclusion inside the CrN matrix of a CrN/Cr_2N film deposited at 650 °C with a 20% nitrogen gas mixture. (e) TEM and (f) HRTEM image of CrN/Cr_2N film deposited at 600 °C with a 20% nitrogen gas mixture. Note the 20 nm × 50 nm hexagonal Cr_2N nanoinclusions.

show a large variation in the electrical resistivity depending on the deposition temperature. Films deposited at 600 °C (sample Cr40-600) show a resistivity of 300 mΩ cm, while as films deposited at 700 °C (sample Cr40-700) show a resistivity of 0.75 mΩ cm (400 times lower). Samples Cr20-600, Cr20-650 and Cr20-700 (deposited with a 20% N_2 gas mixture) show a competing relationship between film deposition temperature and electrical resistivity, as the low nitrogen mixture during the deposition process leads to the formation of the metallic secondary phase Cr_2N. Although single phase Cr_2N has a relatively low electrical resistivity of 0.05 mΩcm, the mixture of CrN and Cr_2N does not decrease the electrical resistivity below that of sample Cr40-700 with a resistivity of 0.75 mΩ cm.

In order to study the secondary phase Cr_2N inside the film, TEM images of single phase CrN (sample Cr40-700) are compared with the CrN/Cr_2N mixture films (sample Cr20-650 and Cr20-600). Figure 4(a) shows a bright field TEM image for CrN films deposited at 700 °C with a 40% nitrogen gas flow mixture (Cr40-700). Figure 4(b) shows the HRTEM image and the selected area electron diffraction (SAED) pattern of the same film, exhibiting epitaxial growth. The observed lattice spacing of 0.23 nm corresponds to the CrN $d_{(111)}$ lattice spacing in the XRD diffraction pattern. Figure 4(c) shows a TEM image of sample Cr20-650 deposited at 650 °C with a 20% nitrogen gas flow mixture. The HRTEM image in figure 4(d) shows that these deposition parameters lead to the formation of 10 × 15 nm nanoinclusions which can be seen residing in the CrN matrix.

Figure 4(e) shows a TEM image of a CrN/Cr_2N film deposited at a lower temperature (sample Cr20-600). The corresponding HRTEM image (figure 4(f)) shows that a decrease in the deposition temperature has caused an increase in the Cr_2N grain size in the film and results in 20 × 50 nm Cr_2N nanoinclusions randomly dispersed in the CrN matrix. These changes also include crystal defects and grain boundaries.

3.3. Thermoelectric properties

Thermoelectric measurements (i.e. the Seebeck coefficient and the electrical resistivity) as a function of temperature were measured to study the effect of the secondary phase Cr_2N when mixed with CrN films which includes Cr40-700, Cr20-600, and Cr20-650. In addition, the Seebeck coefficient and electrical resistivity of single phase Cr_2N was also measured as a reference (sample Cr20-700). Figure 5(a) shows the temperature dependent electrical resistivity of all measured samples. For single phase CrN and CrN with small-sized nanoinclusions (Cr40-700 and Cr20-650) the resistivity increases with increasing temperature (metallic-like behavior) and peaks near 700 K before showing a decrease. This metal-like behavior is unexpected for semiconductors. For the CrN/Cr_2N films with 20 nm× 50 nm nanoinclusions (Cr20-600), the resistivity peaks at temperatures near 550 K before showing the decrease.

Figure 5(b) presents the Seebeck coefficients as a function of temperature for the investigated samples. The results show that small-sized (10 nm × 15 nm particles) Cr_2N phase impurities does not have a large effect on the Seebeck coefficient and the values are approximately the same as single phase CrN with a -230 μ VK^{-1} Seebeck coefficient at 600 K. The Seebeck coefficient of samples with large-sized (20 nm ×

50 nm particles) Cr_2N impurities is measured to be approximately $-160\ \mu VK^{-1}$ and is almost constant with temperature. All measurements show negative Seebeck coefficients characteristic of n-type semiconducting behavior.

Figure 5(c) shows the power factor for all of the mentioned samples. The results show power factors as high as 5.0×10^{-3} $Wm^{-1} K^{-2}$ at room temperature for single phase and low impurity CrN films and 1.5×10^{-3} $Wm^{-1} K^{-2}$ for the film with large amounts of Cr_2N. The power factor decreases with temperature (because of the electrical resistivity increase) and drops to 2.5×10^{-3} $Wm^{-1} K^{-2}$ near 800 K. Additional measurements on single phase CrN do not show any major changes in either the thermoelectric properties or the XRD pattern.

Table 1 also includes the temperature-dependent Hall carrier concentration results for the mentioned samples at room temperature and 800 K. As expected, there is a steady increase in the samples charge carrier concentration depending on the phase, starting from 0.39×10^{19} cm^{-3} for CrN and increasing up to 8.17×10^{22} cm^{-3} for Cr_2N (room temperature measurements). These results stem from the respective semiconducting and metallic properties.

Finally, modulated thermoreflectance microscopy was used to measure the thermal conductivity of single phase CrN and single phase Cr_2N at room temperature. The results show that epitaxial and semiconducting CrN (with a reduced number of defects and grain boundaries) has a thermal conductivity of approximately 4.0 $Wm^{-1} K^{-1}$ while as metallic Cr_2N showed a value of approximately 12.0 $Wm^{-1} K^{-1}$.

4. Discussion

4.1. Film growth and structure

It is well known that higher deposition temperatures lead to enhanced adatom mobility and grain boundary diffusion resulting in grain coalescence and coarsening [51]. As a result, higher deposition temperatures could lead to a decrease in the defect density and grain boundaries (which affect electron mobility by scattering) leading to better electrical conductivity. This could explain the large power factor of sample Cr40-700 compared to previously reported power factors of polycrystalline bulk samples [52]. It should be noted that the CrN (1 1 1) peak belonging to Cr40-600, Cr40-650 and Cr40-700 all show Laue oscillations (layer thickness fringes). The Laue oscillation on a specific diffraction peak appears when the film presents a smooth surface and this can be used to calculate the film thickness [53]. By using the equation $t = \frac{\lambda(n_2-n_1)}{2(\sin\theta_2-\sin\theta_1)}$ for two consecutive fringes, film thickness can be calculated where t is film thickness, λ is the x-ray wavelength, θ is the diffraction angle of the fringe and n is the fringe number. In our case, Cr40-600 is estimated to be 282 nm, Cr40-650 is estimated to be 284 nm, and Cr40-700 is estimated to be 289 nm, consistent with film thicknesses determined from cross-sectional SEM images.

When the films are deposited with a 20% nitrogen gas mixture, deposition temperature also affects film phase purity. The film deposited at 600 °C has large-sized Cr_2N grains compared to the film deposited at 650 °C. On the other hand, the film deposited at 700 °C is single phase Cr_2N. This discrepancy may originate from the slightly lower deposition temperature of 600 °C ($k_BT_{873\,K} = 0.0752$ eV) compared to that of 650 °C ($k_BT_{923\,K} = 0.0795$ eV) which could prevent the nitrogen species incorporation into the octahedral spacing due to the 0.0043 eV difference. Thus, the nitrogen deficiency in the film will lead to the preferred formation of Cr_2N. A preliminary formation energy estimate (based on 0 K first principles calculations) from the Materials Project website [54] for CrN is -0.527 eV, while for Cr_2N is -0.523 eV (a 0.004 eV difference). Increasing the temperature from 600 °C to 650 °C will cover this energy difference for the nitrogen species to reside in the interstitial spacing, but the shortage of sufficient nitrogen gas flow will still cause a small amount of Cr_2N to remain in the film. However, films deposited at 700 °C in a nitrogen deficient ambience will form single phase Cr_2N as the preferred phase.

4.2. Thermoelectric properties

Based on previous studies regarding the effects of nanoinclusions in thermoelectric material [55, 56], it can be hypothesized that the metallic Cr_2N inclusions can act as a charge carrier injector. This should lead to a reduction in the electrical resistivity. Despite this, the film deposited at 600 °C (which has larger nanoinclusions and a 7 times larger charge carrier density) has a higher resistivity compared to the film deposited at 650 °C. The relative TEM image (figure 4(e)) shows that the film with large-sized nanoinclusions also includes multiple crystal grains and grain boundaries which can scatter the charge carriers and increase the electrical resistivity.

However, the most intriguing result is the anomalous electrical resistivity of CrN and CrN/Cr_2N (figure 5(a)). Unlike normal semiconducting behavior where resistivity decreases with temperature, the electrical resistivity of under-stoichiometric CrN and CrN/Cr_2N films increases with temperature. This behavior contrasts with the Seebeck coefficient values which matches that of n-type semiconducting. A likely explanation is that the nitrogen vacancies are acting as donors by greatly increase the charge carrier density, creating non-zero quasi-metallic density of states at the Fermi level for the sample [57, 58]. In this case, a rise in the temperature will probably enhance electron–electron scattering resulting in a small decrease in the conductivity values.

Thermal conductivity measurements show that sample Cr40-700 has a room temperature thermal conductivity of 4.0 $Wm^{-1} K^{-1}$. This is the upper value in CrN thermal conductivity where electron and phonon scattering are minimized. Thus, an estimated zT value at room temperature for single phase CrN thin films would be less than 0.4.

As for the Cr_2N film (sample Cr20-700), its metallic properties result in a near-zero Seebeck coefficient which is not suitable for thermoelectrics. However, Cr_2N also shows a relatively low thermal conductivity value with good electrical conductivity and can be further studied for other applications such as diffusion barriers [59] or hard coatings [60].

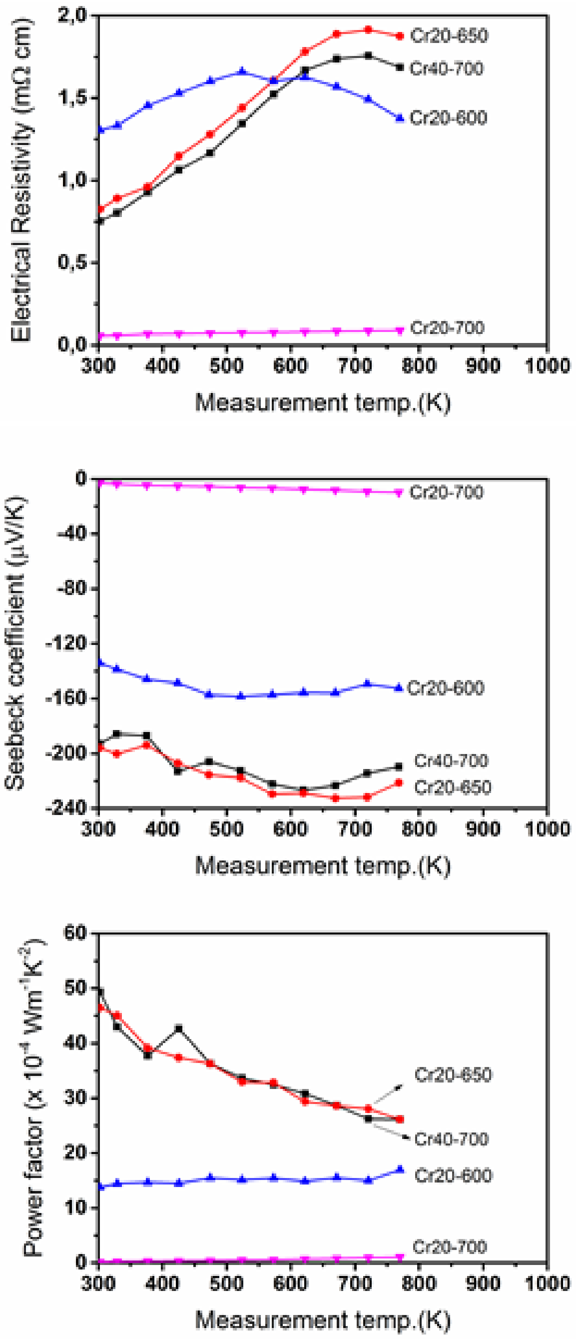

Figure 5. (a) Electrical resistivity, (b) Seebeck coefficient and (c) power factor measurements of single phase CrN and CrN/Cr_2N films with high and low amounts of phase impurities according to the nanoinclusion size. Single phase (and metallic) Cr_2N is also included as a reference material.

5. Conclusions

In summary, chromium nitride thin film synthesis and characterization is reported. Deposition temperatures and gas flow mixtures can be used to change the properties of the film (i.e. Seebeck coefficient, electrical conductivity) by altering the crystal microstructure and/or adding secondary phases. Low nitrogen gas flow mixture will result in the formation of a secondary phase—hexagonal Cr_2N—which takes shape in the form of randomly dispersed nanoinclusions and embedded in a CrN matrix.

Single phase CrN and CrN/Cr_2N films (with small amounts of Cr_2N phase impurities) show thermoelectric properties with the power factor reaching a maximum value of 5.0×10^{-3} $Wm^{-1}K^{-2}$ at 300 K and 2.5×10^{-3} $Wm^{-1}K^{-2}$ near 800 K. The maximum Seebeck coefficient is measured to be $-230\,\mu VK^{-1}$ at 600 K. The room temperature thermal conductivity for the single phase CrN film is measured to be 4.0 $Wm^{-1}\,K^{-1}$. CrN thin films show an interesting behavior of increasing electrical resistivity with temperature (which is the opposite behavior for semiconductors). Also, adding metallic Cr_2N nanoinclusions to the CrN matrix increases the electrical resistivity of the film due to the increased number of grain boundaries and crystal defects. Thus, for future research, it would be advisable to alloy CrN with a metallic compound that shares the same rock-salt cubic crystal structure in order to prevent the formation of such defects. This could lead to an enhancement of the power factor and thermoelectric figure of merit.

Acknowledgments

The authors acknowledge funding from the European Research Council under the European Community's Seventh Framework Programme (FP/2007-2013)/ERC grant agreement no. 335383, the Swedish Government Strategic Research Area in Materials Science on Functional Materials at Linköping University (Faculty Grant SFO-Mat-LiU No. 2009 00971), the Swedish Foundation for Strategic Research (SSF) through the Future Research Leaders 5 program, the Knut and Alice Wallenberg Foundation under the Wallenberg Academy Fellows program, and the Swedish Research Council (VR) under project no. 2016-03365. N V Nong would like to thank the funding support from European Union's Seventh Framework Programme and the Danish Innovation Fund for the NanoCaTe (grant agreement No. 604647) and CTEC (No. 1305-00002B) projects. We also thank Jörgen Bengtsson for his help with the AFM measurements.

ORCID iDs

M A Gharavi https://orcid.org/0000-0003-4833-9233
A le Febvrier https://orcid.org/0000-0002-3059-7392
P Eklund https://orcid.org/0000-0003-1785-0864

References

[1] Williams S, Tipper J L, Ingham E, Stone M H and Fisher J 2003 *Proc. Inst. Mech. Eng.* **217** 155
[2] Hones P, Martin N, Regula M and Lévy F 2003 *J. Phys. D: Appl. Phys.* **36** 1023
[3] Swadzba L, Maciejny A, Formanek B, Liberski P, Podolski P, Mendala B, Gabriel H and Poznanska A 1996 *Surf. Coat. Technol.* **78** 137
[4] Panjan P, Navinšek B, Cvelbar A, Zalar A and Milošev I 1996 *Thin Solid Films* **282** 298
[5] Sanjinés R, Hones P and Lévy F 1998 *Thin Solid Films* **332** 225
[6] Wei G, Rar A and Barnard J A 2001 *Thin Solid Films* **399** 460
[7] Quintela C X *et al* 2015 *Adv. Mater.* **27** 3032

[8] Kerdsongpanya S, Sun B, Eriksson F, Jensen J, Lu J, Koh Y K, Nong N V, Balke B, Alling B and Eklund P 2016 *J. Appl. Phys.* **120** 215103

[9] Jankovský O, Sedmidubský D, Huber Š, Šimek P and Sofer Z 2014 *J. Eur. Ceram. Soc.* **34** 4131

[10] Jagannadham K 2015 *J. Vac. Sci. Technol.* A **33** 031514

[11] Eklund P, Kerdsongpanya S and Alling B 2016 *J. Mater. Chem.* C **4** 3905

[12] Constantin C, Haider M B, Ingram D and Smith A R 2004 *Appl. Phys. Lett.* **85** 6371

[13] Zhang X Y and Gall D 2010 *Phys. Rev.* B **82** 045111

[14] Browne J D, Liddell P R, Street R and Millis T 1970 *Phys. Status Solidi* **1** 715

[15] Herle P S, Hegde M, Vasathacharya N, Philip S, Rao M R and Sripathi T 1997 *J. Solid State Chem.* **134** 120

[16] Herwadkar A and Lambrecht W R L 2009 *Phys. Rev.* B **79** 035125

[17] Alling B, Marten T and Abrikosov I A 2010 *Phys. Rev.* B **82** 184430

[18] Gall D, Shin C-S, Haasch R T, Petrov I and Greene J E 2002 *J. Appl. Phys.* **91** 5882

[19] Yang J and Caillat T 2006 *MRS Bull.* **31** 224

[20] Brown T J, Idoine N E, Raycraft E R, Shaw R A, Hobbs S F, Everett P, Deady E A and Bide T 2018 World Mineral Production 2012–16 *British Geological Survey* (Keyworth, Nottingham: BGS Publications)

[21] Amatya R and Ram R J 2012 *J. Electron. Mater.* **41** 1011

[22] Snyder N W 1961 *Energy Conversion for Space Power* (New York: Academic)

[23] Ravich Y I, Efimova B A and Smirnov I A 1970 *Semiconducting Lead Chalcogenides* (Berlin: Springer)

[24] Vasilevskiy D, Masut R A and Turenne S 2012 *J. Electron. Mater.* **41** 1057

[25] Tritt T M 2011 *Annu. Rev. Mater. Res.* **41** 433

[26] Shakouri A 2011 *Annu. Rev. Mater. Res.* **41** 399

[27] Kerdsongpanya S, Nong N V, Pryds N, Žukauskaite A, Jensen J, Birch J, Lu J, Hultman L, Wingqvist G and Eklund P 2011 *Appl. Phys. Lett.* **99** 232113

[28] Kerdsongpanya S, Alling B and Eklund P 2012 *Phys. Rev.* B **86** 195140

[29] Burmistrova P V, Maassen J, Favaloro T, Saha B, Salamat S, Koh Y R, Lundstrom M S, Shakouri A and Sands T D 2013 *J. Appl. Phys.* **113** 153704

[30] Burmistrova P V, Zakharov D N, Favaloro T, Mohammed A, Stach E A, Shakouri A and Sands T D 2015 *J. Mater. Res.* **30** 626

[31] Kerdsongpanya S, Hellman O, Sun B, Koh Y K, Lu J, Nong N V, Simak S I, Alling B and Eklund P 2017 *Phys. Rev.* B **96** 195417

[32] Kerdsongpanya S, Alling B and Eklund P 2013 *J. Appl. Phys.* **114** 073512

[33] Saha B, Garbrecht M, Perez-Taborda J A, Fawey M H, Koh Y R, Shakouri A, Martin-Gonzalez M, Hultman L and Sands T D 2017 *Appl. Phys. Lett.* **110** 252104

[34] Tureson N, Nong N V, Fournier D, Singh N, Acharya S, Schmidt S, Belliard L, Soni A, le Febvrier A and Eklund P 2017 *J. Appl. Phys.* **122** 025116

[35] Schroeder J L, Ewoldt D A, Amatya R, Ram R J, Shakouri A and Sands T D 2014 *J. Microelectromech. Syst.* **23** 672

[36] Saha B *et al* 2016 *Phys. Rev.* B **93** 045311

[37] Rawat V, Koh Y K, Cahill D G and Sands T D 2009 *J. Appl. Phys.* **105** 024909

[38] Quintela C X, Rodríguez-González B and Rivadulla F 2014 *Appl. Phys. Lett.* **104** 022103

[39] Eriksson F, Johansson G A, Hertz H M and Birch J 2002 *Opt. Eng.* **41** 2903

[40] Horcas I, Fernandez R, Gomez-Rodriguez J M, Colchero J, Gomez-Herrero J and Baro A M 2007 *Rev. Sci. Instrum.* **78** 013705

[41] Haasch R T, Lee T-Y, Gall D, Greene J E and Petrov I 2000 *Surf. Sci. Spectra.* **7** 204

[42] Pottier L 1994 *Appl. Phys. Lett.* **64** 1618

[43] Li B, Roger J-P, Pottier L and Fournier D 1999 *J. Appl. Phys.* **86** 5314

[44] Plamann K, Fournier D, Forget B C and Boccara A C 1996 *Diamond Relat. Mater.* **5** 699

[45] Frétigny C, Roger J P, Reita V and Fournier D 2007 *J. Appl. Phys.* **102** 116104

[46] Frétigny C, Duquesne J-Y, Fournier D and Xu F 2012 *J. Appl. Phys.* **111** 084313

[47] Xu F, Frétigny C, Fournier D, Belliard L, Vincent S, Perrin B, Martin S, Secouard C and Duquesne J-Y 2013 *J. Appl. Phys.* **113** 244304

[48] Frétigny C, Duquesne J-Y and Fournier D 2015 *Int. J. Thermophys.* **5–6** 1281

[49] Gall D, Shin C-S, Spila T, Odén M, Senna M J H, Greene J E and Petrov I 2002 *J. Appl. Phys.* **91** 3589

[50] Eklund P, Högberg H and Hultman L 2007 *Phys. Status Solidi* **1** 113

[51] Petrov I, Barna P B, Hultman L and Greene J E 2003 *J. Vac. Sci. Technol.* A **21** S117

[52] Quintela C X, Rivadulla F and Rivas J 2009 *Appl. Phys. Lett.* **94** 152103

[53] Birkholz M 2006 *Thin Film Analysis by X-Ray Scattering* (New York: Wiley)

[54] Jain A *et al* 2013 *APL Mater.* **1** 011002

[55] Kim W, Singer S L, Majumdar A, Vashaee D, Bian Z, Shakouri A, Zeng G, Bowers J E, Zide J M O and Gossard A C 2006 *Appl. Phys. Lett.* **88** 242107

[56] Kim W, Zide J, Gossard A, Klenov D, Stemmer S, Shakouri A and Majumdar A 2006 *Phys. Rev. Lett.* **96** 045901

[57] Mozafari E, Alling B, Steneteg P and Abrikosov I A 2015 *Phys. Rev.* B **91** 094101

[58] Zhang X Y, Chawla J S, Howe B M and Gall D 2011 *Phys. Rev.* B **83** 165205

[59] Chun J-S, Petrov I and Greene J E 1999 *J. Appl. Phys.* **86** 3633

[60] Yan M F and Chen H T 2014 *Comput. Mater. Sci.* **88** 81